Saturation Consideration in Modeling of the Induction Machine using Subdomain Technique to Predict Performance

Emad Roshandel, *Student member, IEEE,* Amin Mahmoudi, *Senior member IEEE*, Solmaz Kahourzade, *Member, IEEE,* and Wen L. Soong, *Member, IEEE*

***Abstract*— In this paper, the analysis of induction machines using five separated subdomains including the rotor slot, rotor slot opening, airgap, stator slot opening, and stator slot regions is considered. The Maxwell equations of each region are solved considering the boundary conditions. Uniform distributions of the current density in the rectangular slots of both the rotor and stator are considered to find the energy of the winding and to calculate the machine inductances using the energy equation. The calculated flux density of each subdomain is used to find the flux distribution. The calculated magnetic flux intensities are required to estimate the saturation level of the motor cores and correct the saturation-related values such as the leakage and magnetizing inductances. The machine core losses are calculated based on the Steinmetz equation at the no-load condition. The calculated inductances and resistances are used in the equivalent circuit of the squirrel-cage induction machine (SCIM) for the performance prediction. The results demonstrate the reliability of the saturation model in the prediction of the saturation influence in a wide range of magnetization levels. The accuracy of the proposed model in the prediction of the performance of the SCIM is validated using 2D and 3D finite element analysis (FEA) results. A sensitivity analysis with 75 different geometries was conducted to show the capability of the model for the performance prediction of a wide range of induction machines.**

***Index Terms*— Induction motor, magnetic vector potential, performance prediction, saturation effect, subdomain model.**

I. Introduction

INDUCTION MACHINES are utilized in many industrial and domestic applications. Therefore, the optimal design of them improves the performance of the electric devices and reduces the energy consumption. Finite element analysis (FEA) is one of the widely used numerical methods for electric machine design studies. The optimal design of electric machines using numerical methods such as FEA is time consuming. Analytical models can predict the electric machine performance faster than numerical methods. Hence, a high-accuracy, reliable analytical method is useful to reduce the time of an optimization study.

The non-numerical methods of the analysis of electric machines are categorized into empirical models and analytical techniques [1-3]. The empirical methods developed based on experiments are not reliable to be applied to all sizes/rated powers of a certain electric machine [4].

The magnetic equivalent circuit (MEC) modeling based on Maxwell equations is another type of the analytical model. Many nodes and reluctances must be considered to prepare an accurate MEC model. The increase of the number of elements in a model not only makes the modelling process more complex but also increases the processing time of the simulation. The MEC accuracy can be improved by consideration of magnetic saturation where the investigation of the nonlinear characteristics of the magnetic materials is required [5].

The consideration of slotting in different parts of the machine has been a difficulty in applying Maxwell's equations [6, 7]. The slotting effect has been modeled using some permeance dependent models [6-8]. The definition of the Carter's coefficient, conformal transformation, and Schwarz-Christoffel mapping techniques are the main contributions of the researchers in modeling the slotted parts in the analytical methods. The use of these techniques makes the analytical model more complex and only provides limited accuracy improvement of the machine performance [9]. These permeance related models are not able to accurately include magnetic saturation [10].

The subdomain models (SDMs) [11, 12] were introduced to consider the slotting effect directly based on the solution of the Maxwell equations. The SDM, which is also called the semi-analytical model, separates the machine geometry into different regions and solves the Maxwell equations for each region based on the boundary conditions. The SDM was comprehensively studied for permanent magnet machines [13].

Due to the difficulty of the eddy-current estimation in the rotor bars of a squirrel-cage induction machines (SCIMs), there is limited literature on this topic [14-19]. The eddy currents are

*Manuscript submitted April 7, 2021. This work was supported by the Australian Research Council Discovery under Grant DP170103343 (Corresponding author: Emad Roshandel).

E. Roshandel, is with the College of Science and Engineering, Flinders University, Adelaide, Australia (emad.roshandel@flinders.edu.au).

A. Mahmoudi is with the College of Science and Engineering, Flinders University, Adelaide, Australia (e-mail: amaminmahmoudi@gmail.com).

S. Kahourzade, is with STEM, University of South Australia, Adelaide, Australia (e-mail: solmaz.kahourzade@unisa.edu.au).

Wen L. Soong is with the School of Electrical and Electronics Engineering, University of Adelaide, Australia (wen.soong@adelaide.edu.au).

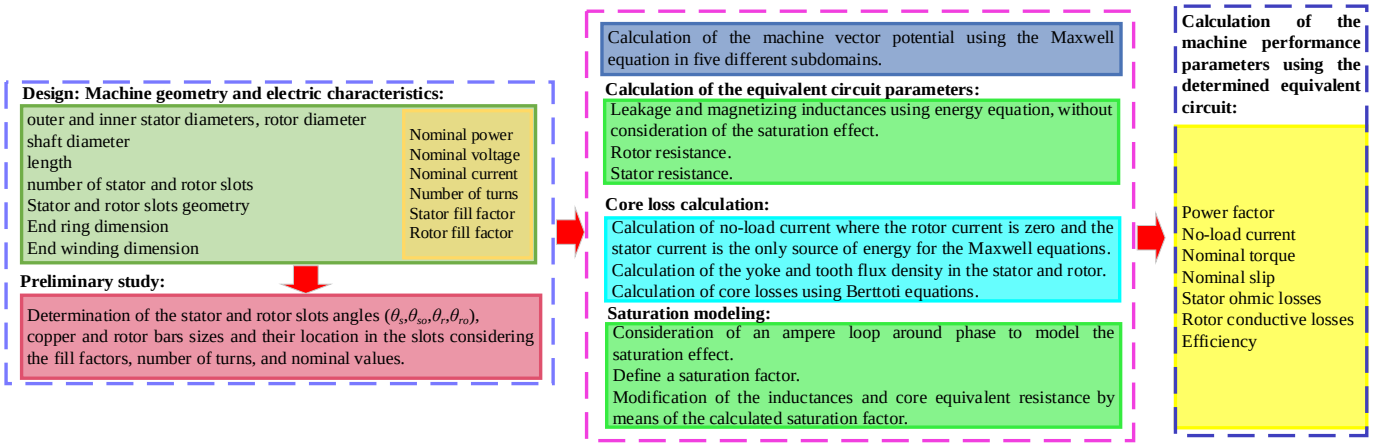

Fig. 1. The flowchart of the proposed analytical model.

calculated by solving the Helmholtz equation [14-17]. The calculation of the eddy currents by estimation of the voltage of the rotor bars using the flux linkage is another technique [18-19]. In all these methods, to predict the SCIM performance, the time stepping method simulates the rotor motion in the SDM of SCIMs. It increases the simulation time due to the consideration of the magnetic field transient.

The previously discussed papers ignore the effect of saturation in the iron parts. The inductance variation caused by the saturation affects the electrical machine's torque generation, torque ripple, power factor, and efficiency. So, the saturation investigation is of great importance to predict the machine performance accurately.

The Cauchy's product theorem was proposed to model the saturation effect by consideration of the permeability of linear soft magnetic material [20]. The authors in [20], explained that the non-linear iron can be modeled based on the proposed method during an iterative procedure. Also, an iterative search-based approach has been introduced in [21] for saturation consideration of the permanent magnet synchronous machine. The utilization of such search-based iterative methods is not computationally efficient. An average equivalent permeability is defined in the saturation model of the permanent magnet motor presented in [22]. This model considered the saturation effect in the back-iron and ignored the rotor part and stator tooth which leads to a lower accuracy in prediction of the saturation.

The analytical modelling of the saturation effect in induction machines is mostly carried out with consideration of the state-space equations and assumption of availability of the stator and rotor currents as the state variables [23-25]. The magnetic nonlinearity is modeled as a function of stator and rotor currents or the magnetizing flux [26, 27]. When the stator and rotor currents are used to develop the saturation function, the magnetizing inductance function should be differentiated with respect to time. The consideration of the magnetizing flux does not need the differentiation, but the simulation will be more complex [28]. These models are application dependent [29] and have been employed for modeling of induction generators, loss calculation, fault analysis, and transient analysis [29, 30]. It is necessary to implement the dynamic model of induction machines to predict the saturation level using these methods.

The calculation of the airgap flux harmonics plays a prominent role in predicting the magnetization level [31]. The accuracy of the airgap flux harmonic technique, introduced in [32], was improved in [33] by separation of the fundamental and third harmonics of the airgap flux density. However, the presented results in [34] were limited to the variation of the saturation factor and the paper did not report the inductance variation influenced by the saturation effect.

The dynamic based models need the motor parameters to simulate and calculate the current harmonics and find the saturation factor at different current. In [35] and [36], a constant saturation coefficient was defined based on the flux linkage of the machine. These models cannot follow the saturation model in all magnetization levels and just consider a correction factor to model the machine at the rated condition. The saturation effect modeling at all magnetization levels is important when the SCIMs are studied in a driving cycle where an inverter drives a SCIM. Thus, there is a lack of an accurate and fast technique for the analytical modeling of the saturation effect over a wide range of voltage and speed.

The skin effect and high order harmonics on the rotor bars has a lower impact on the performance of the machine at smaller slips. In [37], it has been shown that the electric equivalent circuit (EEC) is a suitable tool to predict the steady-state performance of the SCIM. Therefore, an accurate calculation of the EEC parameters enables predicting the SCIM performance properly. Hence, instead of the calculation of the eddy current of the rotor bars studied in [14-19], the proposed model uses the EEC to predict the rotor current at the steady-state operation. The use of EEC increases the speed of the performance estimation because it does not need the time-stepping technique for calculation of the field transients.

In this paper, the Maxwell equations are solved in five subdomains to consider the rotor, airgap, and stator slotted parts like the considered subdomains in [17]. According to the flowchart of the proposed analytical model presented in Fig. 1, the magnetic vector potentials (MVPs) are used to find the EEC inductances using the energy equation and also the core losses. The core loss resistance is computed using the calculated iron loss from the SDM. The EEC is completed by calculation of the rotor and stator resistance based on the sizing equations.

TABLE I. COMPARISON OF THE CONTRIBUTIONS OF THIS STUDY WITH PREVIOUS SDM MODELS OF SCIM.

Ref. no.	Reported performance					magnetic flux density	saturation consideration
	current	torque	core loss	power factor	efficiency		
[14], [15], [16]	✓	✓	✗	✗	✗	✓	✗
[17], [18]	✓	✓	✗	✗	✗	✓	✗
[19]	✓	✓	✗	✗	✗	✓	✗
[38]	✓	✓	✓	✓	✓	✓	✗
This paper	✓	✓	✓	✓	✓	✓	✓

This paper is the continuation of our earlier work presented in [38]. Compared to [38], firstly, the calculation of the EEC inductances in this paper using the energy equations is improved by consideration of the mutual inductance between the stator windings. This improves the accuracy of the calculated inductances from the MVPs. Secondly, a saturation model based on the calculated MVPs in the no-load condition is introduced. It uses a saturation factor to correct the calculated values of the EEC inductances which improves the performance prediction capability of the model. To the best of the authors' knowledge, the proposed saturation model is the only saturation model in the modelling of the SCIMs based on the subdomain techniques. Compared to the previous literature which estimated the saturation level using the dynamics model of the system, the proposed model predicts the saturation without dynamics analysis. This leads to improvement of calculation speed by eliminating time stepping analysis which has been necessary for the former subdomain models.

Table I compares the contribution of the paper with the former SDM based studies and demonstrates that the proposed model includes the calculation of the saturation model compared to the previously introduced models. The presented results show the capability of the model in the prediction of the saturation effect at different magnetization levels. Also, the core loss, efficiency, and power factor of the SCIMs which has not been reported in the most previous SDM models, are reported in this paper.

II. THE PROPOSED METHOD

The proposed model consists of three main calculation steps to model an SCIM and assess its performance. According to Fig. 1, the machine geometry and electrical characteristics of the machine are given as the initial values of the model. In the next step, the quasi-magnetostatic equations of the machine are obtained. Finally, a saturation factor is defined based on the consideration of an Ampere loop over a pole. The core loss at no-load is calculated to find the core loss resistance of the EEC.

A. The quasi-magnetostatics problem

The considered regions for the definition of the magnetostatic problem are shown in Fig. 2. All the slotted parts consisting of the rotor bars, rotor slot opening, airgap, stator slot opening, and rotor slots are investigated in separate subdomains. The MVP is formulated by the Poisson's equation shown in (1) where $\boldsymbol{\mu_0}$ is the magnetic permeability of air and $\boldsymbol{J}$ shows the current density.

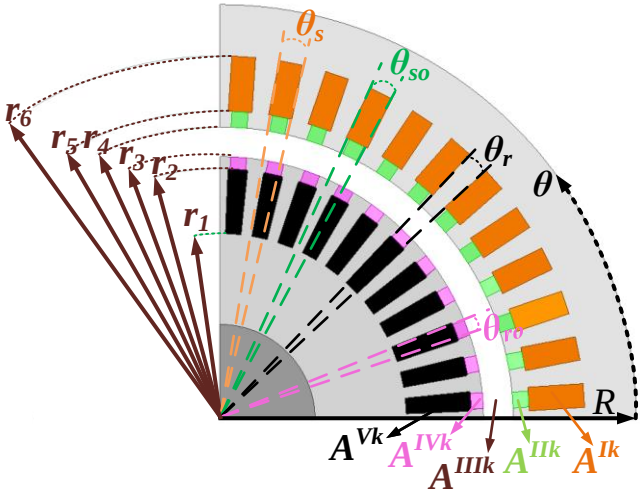

θ_s: slot angles of the stator
θ_{so}: slot opening angle of the stator
r_1 to r_6: the radius of the different subdomains
θ_r: slot angles of the rotor
θ_{ro}: slot opening angle of the rotor
A^{Ik} to A^{Vk}: the magnetic vector potentials inside of each subdomain

Fig. 2. The cross-section of the studied SCIM illustrating the five subdomains and parameters used to write the Maxwell equations in the $R-\theta$ plane.

$$\nabla^2 A = \begin{cases} -\mu_0 J & \text{Through the stator and rotor slots} \\ 0 & \text{Otherwise} \end{cases} \quad (1)$$

The boundary conditions of the different subdomains are obtained based on the continuity of the magnetic flux density and Ampere's law. We have previously discussed the procedure of the derivation of the magnetic vector potentials in each subdomain and the details of the boundary conditions in an earlier paper [38]. According to the presented equations (17)-(22) in [38], the MVPs consist of three different matrices called the geometry (G), excitation (K) dependent, and unknown variables matrices (X). The calculation of the unknown variables using G and K allows the computation of the MVPs for each excitation and geometry.

It was shown that the matrix $\boldsymbol{G}$ is independent from the variation of the excitation and needs to be calculated only once for a certain geometry. As shown in (2), the unknown variables of the magnetic vector potentials in each subdomain are updated based on the current density of the stator windings and rotor bars.

$$\boldsymbol{X} = \boldsymbol{G^{-1}K} \quad (2)$$

The unknown variables and consequently MVPs can be updated for each set of excitations. This characteristic of the $\boldsymbol{K}$ matrix is used to write an equation set derived from the energy equation with five unknown variables (i.e., the turn-ratio ($\boldsymbol{n_{rs}}$), stator and rotor leakage inductance, the magnetizing inductance, and the mutual inductance between the stator windings). Five equations are needed to find these five unknowns. According to the energy equation presented in (3), the magnetic energy results from the integration of the products of half of the current density by MVP's over the volume of the slots.

$$\boldsymbol{W_m} = \frac{1}{2}\sum_{k}\iiint_{v}\left(\boldsymbol{j_{sk}A^{Ik}} + \boldsymbol{j_{rk}A^{Vk}}\right)\boldsymbol{dv} \quad (3)$$

In (3), $\boldsymbol{j_{sk}}$ and $\boldsymbol{j_{rk}}$ are the stator and rotor current density of the k^{th} slot in the stator and rotor slot subdomains. If the saturation

effect is ignored, the energy equation can be expanded as below:

$$W_m = \frac{3}{2}\Big(\frac{1}{2}(L_{ls} + \beta M_{ss} + L_m)i_{ms}^2 + \frac{1}{2}(L'_{lr} + L_m)n_{rs}^2 i_{mr}^2 + n_{rs}L_m i_{mr} i_{ms}\Big) \quad (4)$$

where L_{ls}, L'_{lr}, and L_m are the stator leakage inductance, rotor leakage inductance referred to the stator side, and the magnetizing inductance, respectively. Also, M_{ss} is the mutual inductances between the stator windings. β is defined to consider the number of the mutual inductances for different current distributions in the windings. The stator and rotor currents are shown by i_{ms} and i_{mr}, respectively. Note that the stator and rotor leakage inductances (i.e., L_{ls}, L'_{lr}), magnetizing inductance (L_m), stator winding mutual inductance (M_{ss}), and the turn-ratio are the five unknowns of these equations which are required to define the EEC parameters used in [38]. According to (4), the calculated values of the inductances are independent of the amplitude of the current (ignoring saturation). So, determination of some arbitrary values for excitation of the windings is possible for the analysis. As such, the current distribution over the slots is important to calculate valid values for the inductances.

In [38], it was assumed that the stator leakage inductance and rotor leakage inductance transformed to the stator side are equal. This enables the definition of three sets of excitations for creation of three equations to find the unknown variables. This assumption is logical especially for analysis of the induction machine at rated condition using the EEC. So, four independent equations are required to find L_{ls}, L_m, M_{ss}, and n_{rs} whereas $L_{ls} = L'_{lr}$.

Considering (4), the summation of the stator leakage and magnetizing inductances are obtained when the rotor current (i_{mr}) is zero and i_{ms} is injected into the stator winding. A single layer winding structure is assumed for the distribution of the current in the slots to simulate this condition. The red solid line (I_{st}) in Fig. 3(a) shows the distribution of stator current for the calculation of the energy by (4). Note that the current of phase C is zero in this excitation and consequently β is 1. So, the calculated energy (W_{ms}) is equal to the summation of the stored energy in the leakage inductance, mutual inductance, and a magnetizing inductance. Considering the rated frequency (f) and the synchronous electrical angular frequency ($\omega = 2\pi f$), the first equation of the four required equations is obtained as follows:

$$X_{ls} + X_{Mss} + X_m = 4\omega W_{ms}/3I_{st}^2 \quad (5)$$

A sinusoidal current (I_{rt}) shown in Fig. 3(b) is distributed in the rotor bars whereas the stator current is zero ($I_{st} = 0$). In this excitation condition, the second term of the energy equation (W_{mr}) is non-zero. It enables writing the second required equation which is presented in (6).

$$X'_{lr} + X_m = 4\omega W_{mr}/(3I_{rt}^2 n_{rs}^2) \quad (6)$$

The third set of the combination of excitation is prepared when the stator slots are supplied by the solid red lines in Fig. 3(a) and rotor bars are excited by the current presented in Fig. 3(b). The resulted equation (W_{mrs}) from this excitation is employed to write the third required equation presented in (7).

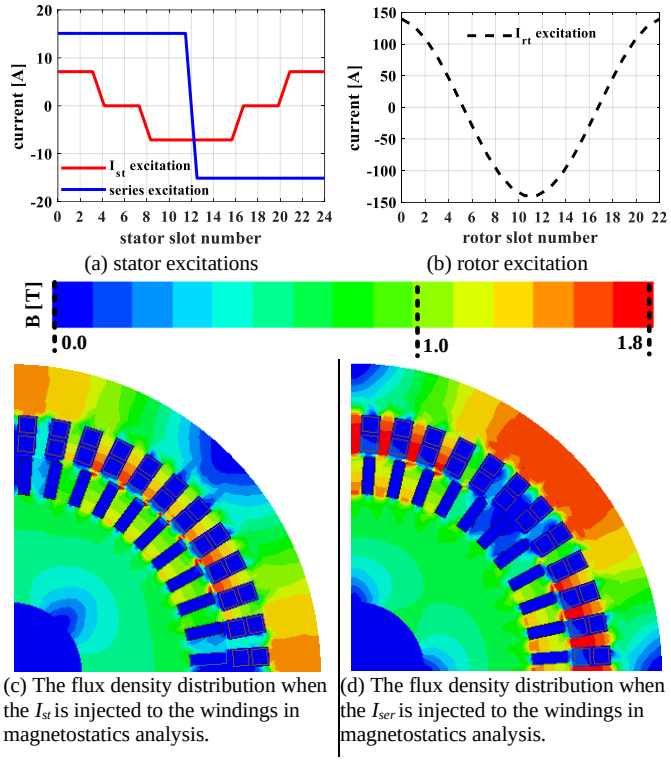

(a) stator excitations (b) rotor excitation

(c) The flux density distribution when the I_{st} is injected to the windings in magnetostatics analysis.

(d) The flux density distribution when the I_{ser} is injected to the windings in magnetostatics analysis.

Fig. 3. (a) and (b): the distributed currents in the stator and rotor slots used to write the energy equations, (c) and (d): flux density distributions.

$$X_m = 2\omega(W_{mrs} - W_{ms} - W_{mr})/(3I_{st}I_{rt}n_{rs}) \quad (7)$$

The above three equations are driven from (4) in different excitation conditions. In the single layer excitation shown with the red line in Fig. 3(a), the flux encompasses a pole (see Fig. 3(c)). Hence, the resulting mutual inductance is the inductance between the windings of phases A and B. If an excitation is defined to create a flux pattern like the single layer winding excitation, the mutual inductance will be equal to the summation of several mutual inductances, leakage inductances, and magnetizing inductance when the machine operates at the no-load condition. The blue line excitation in Fig. 3(a) which is called the series excitation (I_{ser}) is defined to calculate the energy from (3). In this excitation, the flux linkage equation is written by (8) and the energy equation calculated from the integral of the flux linkage is shown in (9).

$$\lambda = L_{ls}I_{sera} + M_{ss}I_{serc} + M_{ss}I_{serb} + L_mI_{sera} + L_{ls}I_{serb} + M_{ss}I_{serc} + M_{ss}I_{sera} + L_mI_{serb} + L_{ls}I_{serc} + M_{ss}I_{sera} + M_{ss}I_{serb} + L_mI_{serc} \quad (8)$$

$$W_{mse} = \frac{3}{2}(L_{ls} + 2M_{ss} + L_m)I_{ser}^2 \quad (9)$$

The resulting energy is equal to the stored energy in the three phase inductances. The flux density distribution presented in Fig. 3(d) shows the similarity of the flux patterns in both excitations (red line and blue lines in Fig. 3(a)) when they are distributed on the stator slots. The calculated energy (W_{mse}) is used as the fourth required equation to write the four-equation system. The relationship between the calculated energy and the inductances is written in (10).

$$X_{ls} + 2X_{Mss} + X_m = 2\omega W_{mse}/3I_{ser}^2 \quad (10)$$

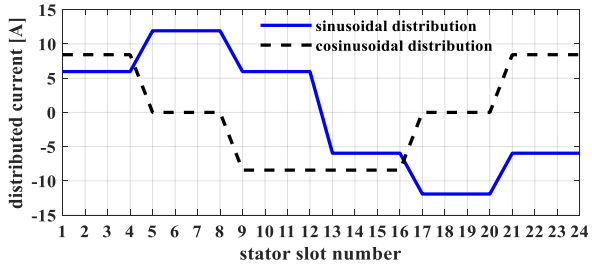

Fig. 4. Sinusoidal and cosinusoidal distribution of the current under a pole used for calculation of the core losses.

All the derived equations (5-7,10) are solved to determine the leakage and magnetizing inductances required for the EEC. The stator and rotor resistances (i.e., $\boldsymbol{R_s}$ and $\boldsymbol{R'_r}$) are other important parameters of the equivalent circuit. The stator resistance is calculated based on the presented equation in (11).

$$\boldsymbol{R_s = (1 + \alpha\Delta\theta)\frac{\rho((r_5 + r_6)\pi/2P + 2L)N_{ss}P}{3\theta_s(r_6^2 - r_5^2)k_{fs}}} \qquad (11)$$

where $\boldsymbol{\alpha}$ is the temperature coefficient and $\boldsymbol{\Delta\theta}$ is the difference of the stator winding temperature with 25˚C. $\boldsymbol{\rho}$ is the resistivity of copper at 25˚C. $\boldsymbol{P}$ represents the number of pole pairs. $\boldsymbol{L}$ and $\boldsymbol{N_{ss}}$ are the stack length and number of stator slots, respectively, and $\boldsymbol{k_{fs}}$ is the fill factor of the windings. The rotor bar resistance ($\boldsymbol{R_b}$) and end-ring equivalent resistance ($\boldsymbol{R_{er}}$) are obtained by (12) where the number of bars is shown by ($\boldsymbol{N_b}$) and the bars and end ring cross section areas are indicated by $\boldsymbol{A_{er}}$, respectively. Aluminum resistivity is shown by $\boldsymbol{\rho_{AL}}$. Also, the rotor fill factor is presented by $\boldsymbol{k_{fr}}$.

$$\begin{aligned} R_b &= \rho_{AL}L_{bar}/\left(\theta_r(r_2^2 - r_1^2)k_{fr}\right) \\ \boldsymbol{R_{er}} &= \boldsymbol{\rho_{AL}}\left(\frac{\boldsymbol{\pi(r_1 + r_2)}}{\boldsymbol{N_b}}\right)\Big/\left(\boldsymbol{A_{er}}\sin^2\left(\frac{\boldsymbol{\pi P}}{\boldsymbol{N_b}}\right)\right) \\ R'_r &= \frac{\mathrm{N_b}}{3}(R_b + 2R_{er})/n_{rs}^2 = R_r/n_{rs}^2 \end{aligned} \qquad (12)$$

In (12), $\boldsymbol{R_r}$, $\boldsymbol{R'_r}$ are rotor resistances seen from the rotor and stator side, respectively. The length of a bar is presented by $\boldsymbol{L_{bar}}$. The core resistance ($\boldsymbol{R_C}$) will be the last element of the EEC which is computed by the calculation of the core loss at the no-load condition. The core loss computation method is discussed in the next section.

B. *Core loss calculation*

The calculation of the core losses can be done using the prepared machine model by applying the time stepping method to the magnetostatic analysis. Due to the rotation of the rotor in the time stepping, the geometry matrix (G) is changed in each rotor position. So, all the calculations must be done again which increases the analysis time. To reduce the simulation time, two different excitations called sinusoidal and cosinusoidal excitation are distributed on the stator slots, separately (see Fig. 4). The flux density in each area (i.e., rotor and stator tooth and yokes) are calculated with each excitation. The maximum value of flux density in each area is chosen to calculate the core loss using the Steinmetz equation similar to the procedure introduced in [38]. The average value of the calculated core losses from the two types of excitations is reported as the core loss.

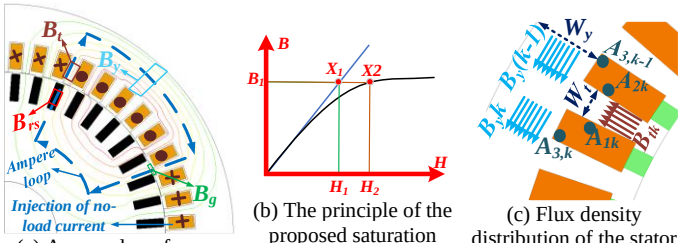

(a) Ampere loop for no-load condition

(b) The principle of the proposed saturation model.

(c) Flux density distribution of the stator yoke and teeth.

Fig. 5. The considered Ampere loop and the strategy of the saturation modelling using the MVPs.

C. *Saturation modeling*

In this section, the saturation effect, which has not been studied in previous SDM related literature about the SCIM, is modelled to increase the accuracy of the calculation of the core loss and machine performance using the SDM and EEC. The magnetic flux density of an ideal core is similar to a motor with a real steel core with a same supply voltage because the flux density is a function of voltage and frequency. Therefore, the magnetic flux density of the motor with the real steel core can be calculated based on its B-H curve. The calculated magnetic field strength are required to estimate the saturation level of the motor cores and correct the saturation-related values in the EEC parameters.

According to Fig. 5(a), an Ampere loop is assumed around a pole in the proposed estimation method of the saturation effect. In an ideal core, with infinite permeability, the ampere-turns produce the magnetic field in the air subdomain. However, in a steel core, in addition to the air subdomain, the iron parts are magnetized according to Ampere's law formulated in (13). So, Ampere's law should be separately written for both iron and air areas.

The flux density in the iron parts depends on the core relative permeability in the stator and rotor teeth and yokes (μ_{rt} and μ_{ry}). According to (13), these values are required to find the exact value of the mmf in each region (i.e., rotor and stator teeth and yokes). In the proposed method, the flux density of the iron parts is calculated when the relative permeability of the core is equal to infinity (shown by X_1 in Fig. 5(b)). Then, the corresponding magnetic field strength (H_2 in Fig. 5(b)) of the calculated flux density based on the real B-H curve is obtained. In other words, the method ignores the relative permeability of the core to find the flux density (i.e., assuming an ideal core) but updates the magnetic field strength value based on the flux density of the real B-H curve.

The ampere-turns (mmf) for the stator/rotor teeth and yoke are demonstrated in (13a) and (13b), respectively. Because some of the rotor/stator teeth under a pole are saturated, especially at higher magnetic loadings, the magnetic flux density of the airgap is usually distorted. Therefore, the average value of the neighboring teeth under a pole is considered to increase the accuracy of the estimation of the magnetic flux density in this modeling method.

The ampere-turns in the air regions consisting of airgap and rotor slots are formulated in (13c) and (13d). In (13c) and (13d), flux density is calculated based on the radial component of the curl of magnetic vector potential in the relevant subdomain.

TABLE II. AMPERE LAW EQUATION FOR A SINGLE POLE AS ILLUSTRATED IN FIG. 6 (THE REQUIRED VECTOR POTENTIALS FOR (13) ARE PRESENTED IN APPENDIX).

$$\sum_k T_s I_{sk} = \underbrace{\int_{in\ core} \vec{H}.\vec{dl}}_{\text{(a) In rotor/stator teeth} \quad \text{(b) In rotor/stator yoke segments}} + \underbrace{\int_{in\ air} \vec{H}.\vec{dl}}_{\text{(c) AIn the airgap region} \quad \text{(d) In the rotor slot}} \tag{13}$$

$$\frac{r_6-r_4}{\mu_0}\left[\frac{(A_{1,\pi s}-A_{2,\pi s})}{\mu_{rts\pi}W_{ts}}+\frac{(A_{1,0s}-A_{2,0s})}{\mu_{rts0}W_{ts}}\right]+\frac{r_3-r_1}{\mu_0}\frac{(A_{1,0r}-A_{2,0r})}{\mu_{rtr\pi}W_{tr}} \quad \frac{2\pi}{N_{ss}\mu_0}\sum_k\left[\frac{A_{3,ks}}{\mu_{rysk}W_{ys}}\right] \quad + \frac{2\pi}{N_b\mu_0}\sum_k\left[\frac{A_{3,ks}}{\mu_{ryrk}W_{yr}}\right]\sum_n\left[\frac{(A_n^{III}-B_n^{III})(1-(-1)^n)}{nP}\right] \quad \sum_n\left[\frac{A_n^{Vk}\theta_r(-1)^n}{n\pi}\right]$$

$$k_{sat} = \left(\int_{in\ core} \vec{H}.\vec{dl} + \int_{in\ air} \vec{H}.\vec{dl}\right) \Big/ \left(\int_{in\ air} \vec{H}.\vec{dl}\right) \tag{14}$$

$$X_m^{new} = X_m/k_{sat};\ X_{ls}^{new} = X_{ls}/k_{sat};\ X_{lr}^{new} = X_{lr}/k_{sat} \tag{15}$$

A_1, A_2, A_3: vector potential values at the positions indicated in Fig 5(c), other indices indicate rotor/stator, and the position of the tooth or yoke segment (e.g., start/end of pole or kth slot).

AT, T_s, I_{sk}: ampere-turns, number of turns per slot, no-load current of turns in kth slot

B_{tr0}: magnetic flux density in the first rotor tooth of a pole, (Fig 5(a))

W_{ts}, W_{tr}, W_{ys}, W_{yr},: width of stator and rotor teeth and yokes, (Fig 5(c))

k_{sat}: saturation factor

$B_{ts\pi}$, B_{ts0}: magnetic flux density in the first and last stator teeth of a pole, (Fig 5(a))

B_{g0}, $B_{g\pi}$: radial component of magnetic flux density in the start and end of a pole, (Fig. 5(a))

B_{yrk}, B_{ysk}, μ_{rt}, μ_{ry}: magnetic flux density of kth stator and rotor segments, relative permeability of the rotor or stator tooth and yoke where *r* and *s* indices indicate the rotor and stator, respectively.

N_{ss}, N_b, P: number of stator slots, rotor bars, and pole pairs.

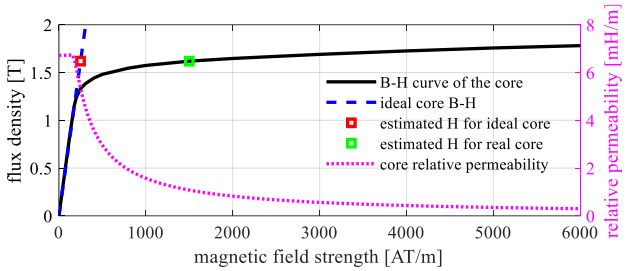

(a) B-H curve of the core lamination materials and the estimated core relative permeability on the basis of the B-H curve.

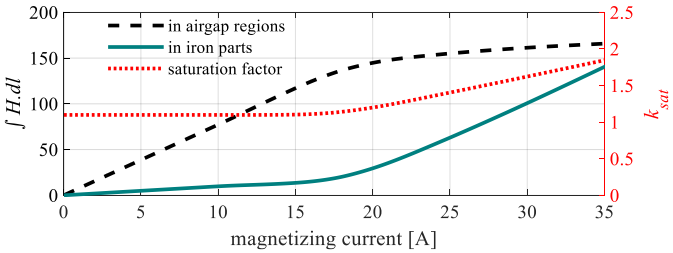

(b) The airgap and iron mmf drops and the saturation factor as a function of magnetizing current.

Fig. 6. The graphical description of the proposed saturation model.

Then, the integral of the magnetic field strength over the closed loop gives the required ampere-turns.

The saturation factor is defined around an Ampere loop which includes the mmf drops in the rotor and stator teeth and yokes as well as the airgap (see Fig. 5(a)). In each saturation level, the magnetic field strength in the iron parts (stator/rotor yokes and teeth) are obtained through the explained procedure for derivation of (13a) and (13b). As the considered Ampere loop shown in Fig. 5(a) includes a rotor slot, the mmf drop in the airgap and rotor slot are obtained using (13c) and (13d). The summation of the calculated mmfs in the core and iron regions results in the numerator of (14). The denominator of (14) is the sum of the calculated mmfs in only the air regions.

As indicated in (15), the EEC magnetizing and leakage reactances are updated by dividing the magnetizing and stator/rotor leakage reactance values by k_{sat}.

The following pseudocode summarizes the procedure of the estimation of the saturation level in SCIMs using the proposed method.

- Find MVPs at each subdomain at no-load condition. The no-load current is found using the calculated reactances before consideration of saturation.
- Calculate A_1, A_2, A_3 using the presented equations in Appendix I at each position in the considered Ampere loop.
- Calculated the required flux densities in each region ($B_{ts\pi}$, B_{ts0}, B_{tr0}, B_{ysk} , B_{yrk}). The relationship of the flux densities with the calculated A_1, A_2, A_3 are formulated in (13a) and (13b).
- Find the magnetic field strength associated with the calculated flux density in each region from the real iron B-H curve.
- Find ampere-turns by multiplication of the obtained magnetic field strength with the length of the iron for each area of iron.
- Calculate the summation of obtained ampere-turns in each region to obtain iron mmf drop (i.e., $\int_{in\ core} \vec{H}.\vec{dl}$).
- Use (13c) and (13d) to find the mmf drop in the air regions (i.e., $\int_{in\ air} \vec{H}.\vec{dl}$).
- Calculate saturation factor using (14).
- Update inductances by means of the obtained saturation factor using (15).

The core B-H characteristic and the estimated permeability of the studied machine is presented in Fig. 6(a) to show the variation of the core permeability as a function of magnetic field strength. The red rectangle in Fig. 6(a) shows the initial flux

density and the corresponding magnetic field strength for an ideal core. The green rectangle is the updated magnetic field strength obtained from the real B-H curve.

Fig. 6(b) shows how the iron and airgap mmfs and saturation factor changes as a function of magnetizing current. At low values of current, the flux density is low, and the iron has a high value of permeability and hence the airgap mmf drop is dominant. At higher values of current, the iron permeability is reduced by saturation which brings about an increase of the iron path reluctance and hence a larger iron mmf drop. The saturation factor is thus near unity at low values of current but increases significantly at higher values of current.

III. Validation of the Proposed Model

A 7.5kW machine with a rated frequency and voltage of 50 Hz and 380 V is considered for the validation of the model. The machine geometry and specifications are reported in Table III. The validation of the proposed model is carried out through a comparative study with FEA results. The software used is Ansys Electromagnetics 2020® [39] which executes the time-domain based FEA model. The time step used is 0.2 ms for both 3D and 2D FEA simulations. A three-phase sinusoidal voltage source was used to model the supply. The effect of inter-bar and in-plane currents are ignored in the FEA model.

The rotor bar end connection resistance (R_{er}) was calculated using (12) and used as the user-defined end ring resistance in 2D FEA model. The effect of the end ring resistance is automatically considered in 3D FEA. Table III includes the height and width of the end rings used for the 3D FEA model. The stator resistance is calculated from (11). The Ansys FEA package uses the Steinmetz equations to estimate the core losses. Similar Steinmetz equations and constants are used to estimate the core losses in the analytical model.

A. Validation of the model in estimation of field and EEC parameters

In the first step, the airgap radial and axial flux density estimated by the proposed method is compared with the 2D and 3D FEA results. Fig. 7 shows that the model can successfully predict the radial and tangential airgap flux density.

To validate the accuracy of the model in the estimation of the saturation level of the core, the magnetization current versus no-load voltage is obtained and compared with the 2D FEA results (see Fig. 8(a)). The variation of the magnetizing and leakage reactances with the magnetizing current is plotted in Fig 8(b). It shows the effectiveness of the saturation factor to estimate a correct value for the inductances.

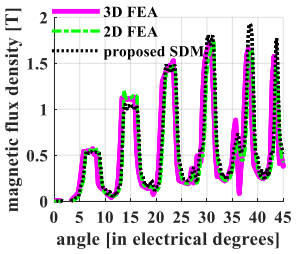

a) Radial flux density

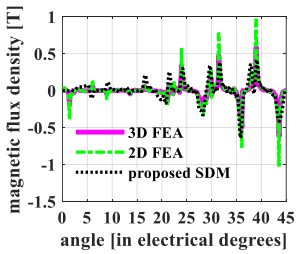

(b) Airgap tangential flux density

Fig. 7. The airgap flux density at the full-load condition, comparison of the analytical results of SDM with 2D and 3D FEA.

TABLE III. THE GEOMETRY AND PROPERTIES OF THE INVESTIGATED MACHINE FOR THE MODEL VERIFICATION.

Core material	M19-24
Number of turns per slot	14
Number of pole pairs	2
Air gap [mm]	0.5
Stack length [mm]	250
Stator outer diameter [mm]	210
Stator inner diameter [mm]	148
Rotor inner diameter [mm]	48
Number of stator slots	48
Number of rotor slots	44
Stator slot height [mm]	12.9
Rotor slot height [mm]	12
Rotor bar length [mm]	254.5
Rotor bar height [mm]	10.8
Stator yoke height [mm]	18.1
Rotor yoke height [mm]	37
Stator wedge height [mm]	0.8
Rotor half-wedge width [mm]	0.5
Rotor inner end ring width [mm]	8
Rotor inner end ring height [mm]	8

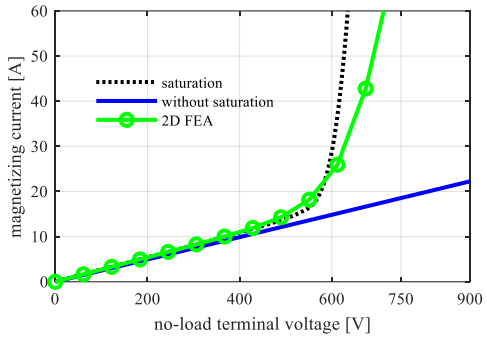

(a) Magnetizing current versus no-load line voltage

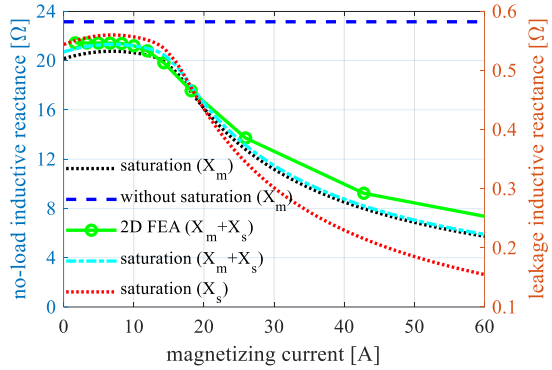

(b) magnetizing and leakage reactance variation vs. magnetizing current changing as the result of core saturation.

Fig. 8. The performance of the proposed SDM in prediction of the core saturation level.

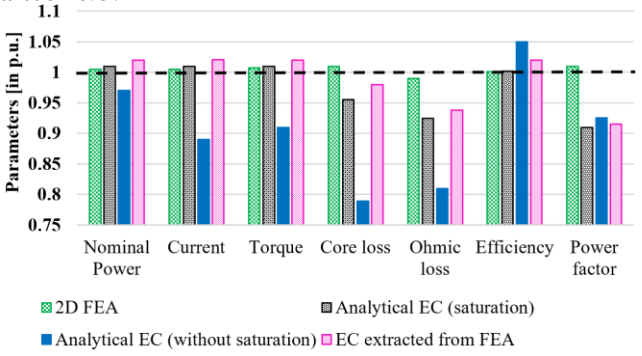

Fig. 9. The performance parameter values compared to the 3D FEA results (dashed line shows the 3D FEA results in p.u.).

TABLE IV. DESIGN PARAMETERS OF THE STUDIED 7.5 KW SCIM

Parameter	Value	Parameter	Value
Nominal power [kW]	7.5	Nominal frequency [Hz]	50
rms line voltage [V]	380	Number of pole pairs	2
Current [A]	17.4	Torque [Nm]	51
Efficiency [%]	83	Speed [rpm]	1418
Core loss [W]	131	Power factor [%]	86
Conductive loss [W]	1381	--	--
Stator winding fill factor	0.49	Rotor fill factor	0.91

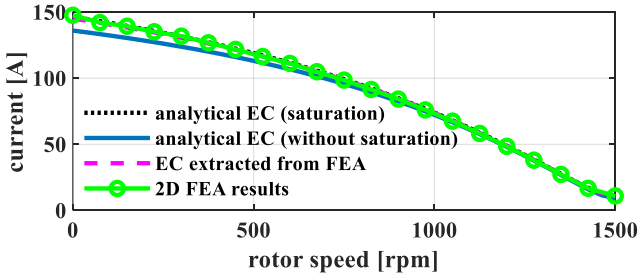

(a) Rotor current versus speed

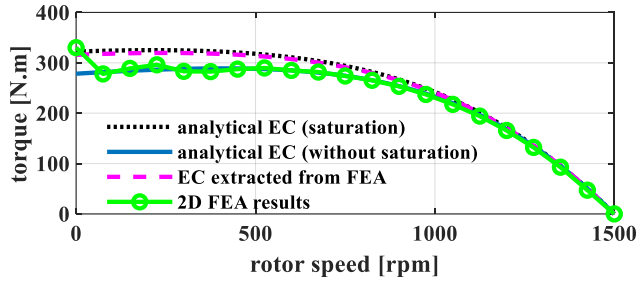

(b) Torque versus speed

Fig. 10. The performance prediction of the machine as a function of speed (comparison of the 2D FEA with the proposed model).

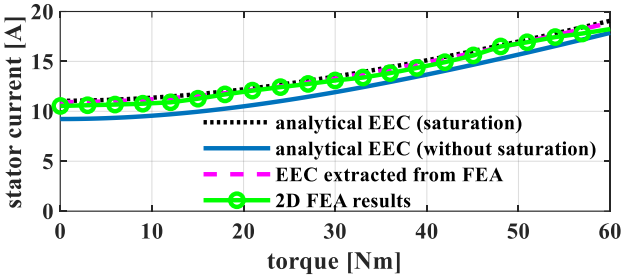

(a) Stator current prediction using EEC.

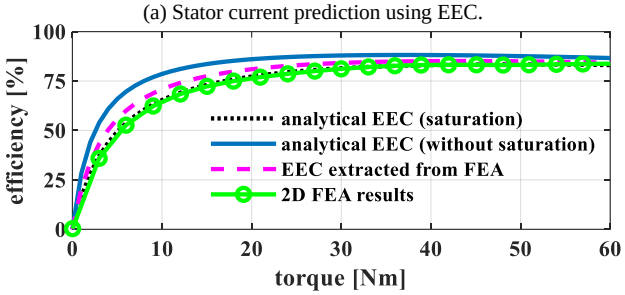

(b) Efficiency prediction using EEC.

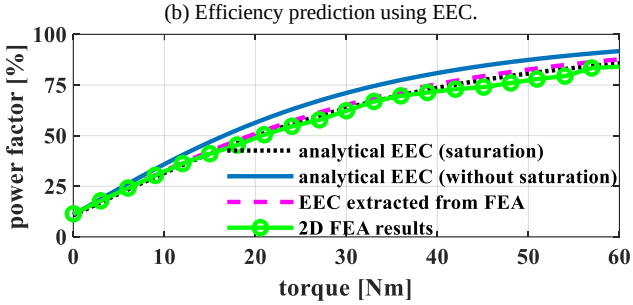

(c) Power factor prediction using EEC.

Fig. 11. Comparison of the predicted performance parameters using the saturation considered model and non-saturation model with the 2D FEA results.

B. Validation of the proposed model in prediction of the performance parameters

The extracted performance parameters of the studied 7.5 kW SCIM from 3D FEA, reported in Table IV, are investigated as the rated values of the machine. Table V shows the calculated values of the equivalent circuit parameters for the case study. Having these parameters enables the calculation of the machine performance parameters using the EEC model used in [38]. A bar graph is provided to compare the results of the proposed model with the conventional analytical model and 2D FEA. The bar graph presented in Fig. 9 demonstrates the proposed model accuracy in the prediction of the SCIM performance. Note that all values are per unitized where the 3D FEA results are considered as the base value.

The stator current and electromagnetic torque against speed of the machine are presented in Fig. 10(a) and (b), respectively. These curves demonstrate the ability of the proposed model to predict the performance parameters. Note that the torque is not completely matched in low speeds because of the rectangular shape of the considered slots which affects the flux paths and increases the high order harmonics at the current of the bars. The crawling effect resulting from the presence of the high-order harmonics of the rotor bar currents cannot be predicted because only fundamental harmonic is considered in EEC model.

The model can be improved by the consideration of the three-cage model [38]. However, the prediction of the torque at lower speeds is not so important when the steady-state loaded performance of a machine is the main objective of the study.

Fig. 11 shows the machine performance with different loads. The EEC results with consideration of the saturation effect has an acceptable accuracy. The current of the machine with consideration of the saturation at no-load matches well with the FEA results. It shows that the magnetizing current and stator leakage inductance are properly calculated. Also, the phase current has a good agreement with the 2D FEA results which shows the appropriate calculation of the rotor branch elements. Fig. 11(b) shows the efficiency variation in different loads and demonstrates the acceptable ability of the saturation model in the calculation of the efficiency. Efficiency can be correctly calculated when the ohmic and core losses are computed correctly. It must be highlighted that the correct estimation of the rotor side losses shows the correct estimation of the slip because the value of the slip determines the amplitude of the current in different loads.

A sensitivity analysis was carried out by changing the machine length, machine outer diameter, airgap, and number of turns resulting in 75 machine design variations. The 2D FEA results of 75 designs are compared with the saturation and non-saturation proposed models as shown in Fig. 12. The results of the analytical model have a good agreement with the results of

TABLE V. EQUIVALENT CIRCUIT PARAMETERS FOR THE STUDIED MODELS AT RATED VOLTAGE.

EEC parameters	SDM model (without saturation consideration)	SDM model (with saturation consideration)	FEA EEC parameters (Results of locked rotor and no-load simulations)
R_s(stator side)	0.4 Ω	0.4 Ω	0.4 Ω
R_r(rotor side)	0.0131 Ω	0.0131 Ω	0.0137 Ω
R'_r (stator side)	0.86 Ω	0.86 Ω	0.90 Ω
X_{ls}(stator side)	0.62 Ω	0.51 Ω	0.48 Ω
X'_{lr}(stator side)	0.62 Ω	0.51 Ω	0.48 Ω
X_m(stator side)	23.1 Ω	19.3 Ω	19.6 Ω
R_c(stator side)	1585 Ω	1310 Ω	1251 Ω

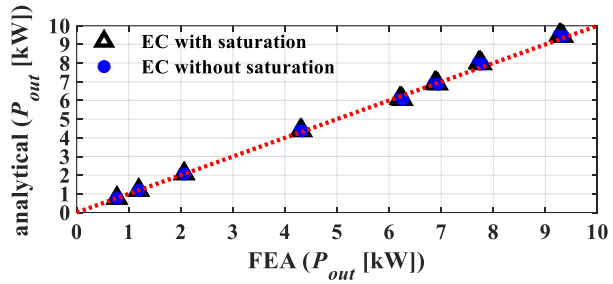

(a) Accuracy validation of the model in prediction of output power.

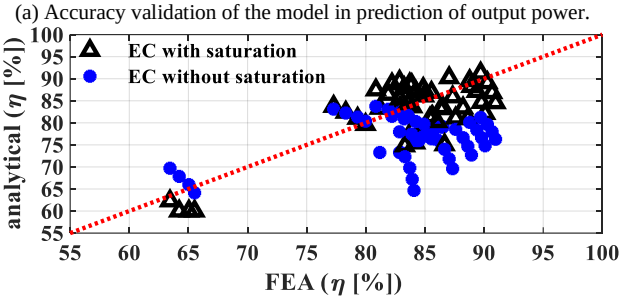

(b) Accuracy validation of the model in prediction of efficiency.

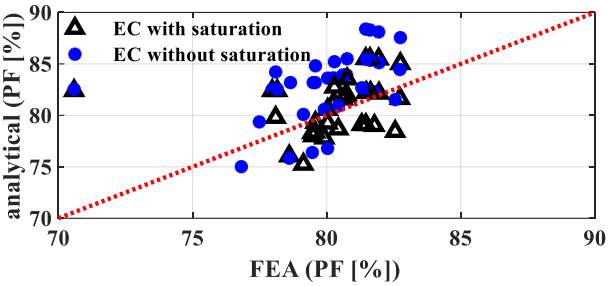

(c) Accuracy validation of model in the prediction of power factor.

Fig. 12. The capability of the saturation and non-saturation models in performance prediction of the induction machines with 75 different geometries via 2D FEA analysis.

the 2D FEA in prediction of the performance parameters. The error of the output power is not exceeding 3% for different geometries. Also, the efficiency error of the proposed model is lower than 5% in all considered geometries which demonstrate the low difference in the value of the machine losses and calculated EEC parameters. Also, error of 10% for the power factor is shown in Fig. 12(c).

The comparison of the required simulation times of the proposed analytical model against 2D FEA demonstrates the analytical model's superiority in terms of speed. A Core i9-7900X (3.30GHz) computer with 128 GB RAM completes each 2D FEA analysis in about 1,000 seconds. In comparison, the performance prediction of a SCIM is completed in 12 seconds using the proposed SDM. The ability of the model for the fast prediction of the machine behavior helps speed up the process of the design of an optimum machine for a specific application.

TABLE VI. COMPARISON OF 3D FEA RESULTS OF THE CASE STUDY WITH AND WITHOUT CONSIDERATION OF THE INTER-BAR CURRENTS.

Rotor core conductivity [MS/m]	0.00		2.00	
Rotor speed [rpm]	0.00	1450	0.00	1450
Torque [Nm]	325.9	36.61	326.6	36.60
Current [A]	134.3	9.28	137.1	9.20
Bar loss [kW]	45.83	0.190	45.56	0.189

C. Validation of the model in prediction of the performance parameters in presence of the inter-bar current

The current which flows through the core material between the adjacent rotor bars is defined as the inter-bar current [40]. The amount of the inter-bar current depends on the conductivity of the rotor core material. The influence of inter-bar currents on the performance of the case study is examined in this part.

As the inter-bar current distribution varies with the slip of the machine [41], the 3D FEA is performed both at locked rotor and 1450 rpm (about three-quarters of rated load). A conductivity of 2 MS/m was used for the core material [41].

The 3D FEA calculated torque, current, and rotor bar losses performance results with and without consideration of the inter-bar currents are reported in Table VI. In general, inter-bar currents were found to produce only a small effect on the performance. The most sensitive parameter is the input current at locked rotor which increased by about 2% when including inter-bar currents. Therefore, the proposed analytical model which ignores the effect of the inter-bar current is fairly accurate.

It should be noted that the proposed model is not intended for transient performance simulation of SCIMs. The time-stepping based models proposed in [15, 16] are slow, but can be used in the real-time simulation when the transient performance is required.

IV. CONCLUSION

An improved subdomain model with capability of the consideration of the saturation effect in iron parts was introduced in this paper. The leakage, magnetizing, and stator mutual inductances were calculated using the magnetic vector potentials (MVPs) obtained from the induction motor (IM) subdomain model. The iron loss was predicted based on the calculated flux density in different parts of the iron based on the magnetic vector potentials at the no-load condition. The electric equivalent circuit was used to study the machine performance. To improve the accuracy of the model, the saturation of the core was estimated using the MVPs at different voltage levels. A saturation factor was defined to find the different values of the saturation dependent components of the IM electric equivalent circuit at different saturation levels. The capability of the model

in the prediction of the machine inductances was validated using finite element analysis (FEA).

The proposed model was used to predict the performance of a 7.5kW induction motor under different loading conditions. The model was compared and validated against the results of 2D and 3D FEA. The results demonstrate that the improved model is more precise compared to the non-saturation model proposed in [38].

A sensitivity analysis was conducted using different machine geometries and used to demonstrate the generality of the model. The effect of inter-bar currents was also investigated using 3D FEA analysis and found to be small. Thus, the proposed model showed acceptable accuracy and fast execution time suitable for optimal design of induction machines with different variables.

In future work, the effect of the eddy-current correction factors, K_r and K_x, for the rotor resistance and reactance can be added to the model to improve the accuracy of the results at lower speeds. The proposed method will be used for optimal design of SCIM. The optimum design will be validated against experimental results from a prototype machine.

V. Appendix I

As discussed above, all the required boundary conditions and magnetic vector potentials have been presented in [38] and the extracted terms to calculate the vector potentials to model the saturation are as follows.

To calculate A_1 and A_2, the magnetic vector potential equation at the stator slot (i.e. equation (17) in [38]) at the middle of the slots with the radius of $\frac{r_4+r_5}{2}$ is investigated. Equation (16) shows the required MVP for calculation of A_1 and A_2. Note that these values are not equal because of the current distribution in all the stator slots.

$$A_{1,2}^k = \sum_n A_n^{Ik}\frac{\theta_s}{n\pi}\frac{\mathrm{P}\left(\frac{n\pi}{\theta_s},\frac{r_5+r_6}{2},r_6\right)}{\mathrm{E}\left(\frac{n\pi}{\theta_s},r_5,r_6\right)}\cos\left(\frac{n\pi}{\theta_s}(\theta-\theta_s^{0k})\right) + a_{1k} - \mu_0 j_v\left(\frac{1}{4}(\frac{r_5+r_6}{2})^2 - \frac{1}{2}r_5^2\ln(\frac{r_5+r_6}{2})\right) \quad (16)$$

where j_v is the current density of the slot and a_{1k} is obtained using the following equation:

$$a_{1k} = a_{2k} - \frac{\mu_0 I_{ks}}{\theta_{so}}\ln r_5 - \sum_n A_n^{Ik}\frac{1}{\theta_{so}}\left(\frac{\theta_s}{n\pi}\right)^2\frac{\mathrm{P}\left(\frac{n\pi}{\theta_s},r_5,r_6\right)}{\mathrm{E}\left(\frac{n\pi}{\theta_s},r_5,r_6\right)}\left[\sin\left(\frac{n\pi}{\theta_s}(\theta_{so}+\theta_{so}^{0k}-\theta_s^{0k})\right)-\sin\left(\frac{n\pi}{\theta_s}(\theta_{so}^{0k}-\theta_s^{0k})\right)\right] + \frac{I_{ks}\mu_0}{\theta_s(r_6^2-r_5^2)}\left(\frac{1}{2}r_5^2 - r_6^2\ln r_5\right) \quad (17)$$

and a_{2k} which depends on the MVPs at the airgap subdomain (i.e. equation (19) in [38]) is achieved by (18).

$$a_{2k} = \frac{\mu_0 I_{ks}}{\theta_{so}}\ln r_4 - \frac{1}{\theta_{so}N_p^2n^2}\left[A_n^{III}\frac{2}{\mathrm{E}\left(nN_p,r_4,r_3\right)} + B_n^{III}\frac{\mathrm{P}\left(nN_p,r_3,r_4\right)}{\mathrm{E}\left(nN_p,r_3,r_4\right)}\right]\left(\cos\left(nNp(\theta_{so}+\theta_{so}^{0k})\right)-\cos(nNp\theta_{so}^{0k})\right) + \frac{1}{\theta_{so}N_p^2n^2}\left[C_n^{III}\frac{2}{\mathrm{E}\left(nN_p,r_4,r_3\right)} + D_n^{III}\frac{\mathrm{P}\left(nN_p,r_3,r_4\right)}{\mathrm{E}\left(nN_p,r_3,r_4\right)}\right]\left(\sin\left(nNp(\theta_{so}+\theta_{so}^{0k})\right)-\sin(nNp\theta_{so}^{0k})\right) \quad (18)$$

A_3 is another required vector potential to calculate the saturation factor which is derived from the stator slots MVPs. Equation (17) in [38] is used to find A_3 by consideration of the maximum radius in the stator yoke. So, A_3 is attained using (19).

$$A_3^k = \sum_n A_n^{Ik}\frac{\theta_s}{n\pi}\frac{2}{\mathrm{E}\left(\frac{n\pi}{\theta_s},r_5,r_6\right)}\cos\left(\frac{n\pi}{\theta_s}(\theta-\theta_s^{0k})\right) + a_{1k} - \mu_0 j_v\left(\frac{1}{2}(r_6)^2 - \frac{1}{2}r_6^2\ln(r_6)\right) \quad (19)$$

The saturation study is conducted in the no-load condition where the rotor current is zero. So, the excitation related term of the equation (21) from [38] is zero and A_{1r} and A_{2r} for the saturation consideration is obtained using (20).

$$A_{1r,2r}^k = \sum_n A_n^{Vk}\frac{\theta_r}{n\pi}\frac{\mathrm{P}\left(\frac{n\pi}{\theta_r},\frac{r_1+r_2}{2},r_1\right)}{\mathrm{E}\left(\frac{n\pi}{\theta_r},r_2,r_1\right)}\cos\left(\frac{n\pi}{\theta_r}(\theta-\theta_r^{0k})\right) + a_{5k} \quad (20)$$

where a_{5k} is calculated using (21).

$$a_{5k} = a_{4k} + \frac{\mu_0 I_{kr}}{\theta_{ro}}\ln r_2 - \sum_n A_n^{Vk}\frac{1}{\theta_{ro}}\left(\frac{\theta_r}{n\pi}\right)^2\frac{\mathrm{P}\left(\frac{n\pi}{\theta_r},r_2,r_1\right)}{\mathrm{E}\left(\frac{n\pi}{\theta_r},r_2,r_1\right)}\left[\sin\left(\frac{n\pi}{\theta_r}(\theta_{ro}+\theta_{ro}^{0k}-\theta_r^{0k})\right)-\sin\left(\frac{n\pi}{\theta_r}(\theta_{ro}^{0k}-\theta_r^{0k})\right)\right] + \frac{I_{kr}\mu_0}{\theta_r(r_2^2-r_1^2)}\left(\frac{1}{2}r_2^2 - r_1^2\ln r_2\right) \quad (21)$$

Based on the solutions of the Maxwell equations, a_{4k} is calculated using the following equation:

$$a_{4k} = -\frac{\mu_0 I_{kr}}{\theta_{ro}}\ln r_3 - \frac{1}{\theta_{ro}N_p^2n^2}\left[A_n^{III}\frac{\mathrm{P}\left(nN_p,r_4,r_3\right)}{\mathrm{E}\left(nN_p,r_4,r_3\right)} + B_n^{III}\frac{2}{\mathrm{E}\left(nN_p,r_3,r_4\right)}\right]\left(\cos\left(nNp(\theta_{ro}+\theta_{ro}^{0k})\right)-\cos(nNp\theta_{ro}^{0k})\right) + \frac{1}{\theta_{ro}N_p^2n^2}\left[C_n^{III}\frac{\mathrm{P}\left(nN_p,r_4,r_3\right)}{\mathrm{E}\left(nN_p,r_4,r_3\right)} + D_n^{III}\frac{2}{\mathrm{E}\left(nN_p,r_3,r_4\right)}\right]\left(\sin\left(nNp(\theta_{ro}+\theta_{ro}^{0k})\right)-\sin(nNp\theta_{ro}^{0k})\right) \quad (22)$$

In (21) and (22) the value of the I_{kr}, which represents the rotor current, is zero for the calculation of the saturation factor

because the saturation factor is determined based on the no-load condition. The rest of the vector potentials required for the calculation of the Ampere loop has been presented in [38].

REFERENCES

[1] Hawley, P. Frederick. "Determination of the Mutual Inductance of End Turns of Induction Motors." PhD diss., *California Institute of Technology*, 1933.

[2] B. Dianati, S. Kahourzade and A. Mahmoudi, "Optimization of Axial-Flux Induction Motors for the Application of Electric Vehicles Considering Driving Cycles," in *IEEE Trans. Ener. Conv.* 2019.

[3] E. Devillers, J. Le Besnerais, T. Lubin, M. Hecquet and J. Lecointe, "A review of subdomain modeling techniques in electrical machines: Performances and applications," 2016 *XXII Int. Conf. Elec. Mach.* (ICEM), Lausanne, pp. 86-92, 2016.

[4] Fan Tao, Luo Jian, Wen Xuhui and Liao Xiaofeng, "A new sizing equation and it's application in electrical machine design," *2011 Int. Conf. Elec. Info. Cont. Eng*., Wuhan, pp. 3890-3893, 2011.

[5] M. Amrhein and P. T. Krein, "Induction Machine Modeling Approach Based on 3-D Magnetic Equivalent Circuit Framework," in *IEEE Trans. Ener. Conv*., vol. 25, no. 2, pp. 339-347, June 2010.

[6] N. Boules, "Two-dimensional field analysis of cylindrical machines with permanent magnet excitation," *IEEE Trans. Ind. Appl.*, vol. IA-20, no. 5, pp. 1267–1277, 1984.

[7] E. Bolte and K. Oberretl, "Three-dimensional analysis of linear motor with solid iron secondary," *Int. Conf. Elec. Mach.* (ICEM), pp. 68–75, 1980.

[8] D. ˇZarko, D. Ban, and T. A. Lipo, "Analytical calculation of magnetic field distribution in the slotted air gap of a surface permanent-magnet motor using complex relative air-gap permeance," *IEEE Trans. Mag.*, vol. 42, no. 7, pp. 1828–1837, 2006.

[9] X. Wang, Q. Li, S. Wang, and Q. Li, "Analytical calculation of air-gap magnetic field distribution and instantaneous characteristics of brushless DC motors," *IEEE Trans. Ener. Conv.*, vol. 18, no. 3, pp. 424–432, 2003.

[10] F. Dubas, K. Boughrara. "New scientific contribution on the 2-D subdomain technique in Cartesian coordinates: taking into account of iron parts," *Math. Comput. Appl.*, vol. 22, no. 1, 2017.

[11] F. Dubas and C. Espanet, "Analytical solution of the magnetic field in permanent-magnet motor taking into account slotting effect," *IEEE Trans. Mag.*, vol. 45, no. 5, pp. 2097–2109, 2009.

[12] Z. Q. Zhu, L. J. Wu and Z. P. Xia, "An Accurate Subdomain Model for Magnetic Field Computation in Slotted Surface-Mounted Permanent-Magnet Machines," in *IEEE Trans. Mag.*, vol. 46, no. 4, pp. 1100-1115, April 2010.

[13] V. Z. Faradonbeh, A. Rahideh, M. M. Ghahfarokhi, E. Amiri, A. D. Aliabad and G. A. Markadeh, "Analytical Modeling of Slotted, Surface Mounted Permanent Magnet Synchronous Motors with Different Rotor Frames and Magnet Shapes," in *IEEE Trans. Mag.*, 2020.

[14] T. Lubin, S. Mezani, and A. Rezzoug, "Analytic Calculation of Eddy Currents in the Slots of Electrical Machines: Application to Cage Rotor Induction Motors," *IEEE Trans. Magn*., vol. 47, no. 11, pp. 4650–4659, 2011.

[15] K. Boughrara, N. Takorabet, R. Ibtiouen, O. Touhami, and F. Dubas, "Analytical Analysis of Cage Rotor Induction Motors in Healthy, Defective and Broken Bars Conditions," *IEEE Trans. Magn*., vol. 51, no. 2, pp. 1-17, Feb. 2015, Art no. 8200317.

[16] L. Roubache, K. Boughrara, and R. Ibtiouen, "Analytical Electromagnetic Analysis of Multi-Phases Cage Rotor Induction Motors in Healthy, Broken Bars and Open Phases Conditions," *Prog. Electromagn. Res. B*, vol. 70, no. October, pp. 113–130, 2016.

[17] E. Devillers, J. Le Besnerais, T. Lubin, M. Hecquet and J. Lecointe, "An Improved 2-D Subdomain Model of Squirrel-Cage Induction Machine Including Winding and Slotting Harmonics at Steady State," in *IEEE Trans. Mag*., vol. 54, no. 2, pp. 1-12, Feb. 2018, Art no. 8100612.

[18] R. L. J. Sprangers, B. L. J. Gysen, J. J. H. Paulides, J. Waarma, and E. A. Lomonova, "Calculation of induced rotor current in induction motors using a slotted semi-analytical harmonic model," *Proc. - 2014 Int. Conf. Electr. Mach. ICEM 2014*, no. 1, pp. 2709–2714, 2014.

[19] R. L. J. Sprangers, J. J. H. Paulides, B. L. J. Gysen, E. a. Lomonova, and J. Waarma, "Electric circuit coupling of a slotted semi-analytical model for induction motors based on harmonic modeling," IEEE Energ. Conv. Cong. Expo. (ECCE), pp. 1301-1308, 2014.

[20] R. L. J. Sprangers, J. J. H. Paulides, B. L. J. Gysen and E. A. Lomonova, "Magnetic Saturation in Semi-Analytical Harmonic Modeling for Electric Machine Analysis," in *IEEE Trans. Mag*., vol. 52, no. 2, pp. 1-10, Feb. 2016, Art no. 8100410.

[21] P. Liang, F. Chai, Y. Li and Y. Pei, "Analytical Prediction of Magnetic Field Distribution in Spoke-Type Permanent-Magnet Synchronous Machines Accounting for Bridge Saturation and Magnet Shape," in *IEEE Trans. Ind. Elec.*, vol. 64, no. 5, pp. 3479-3488, May 2017.

[22] J. Wang, H. Lin, S. Fang and Y. Huang, "A General Analytical Model of Permanent Magnet Eddy Current Couplings," in *IEEE Trans. Mag.*, vol. 50, no. 1, pp. 1-9, Jan. 2014, Art no. 8000109.

[23] J. M. F. de Jesus, "A model for saturation in induction machines," in *IEEE Trans. on Energ. Conv.*, vol. 3, no. 3, pp. 682-688, Sept. 1988.

[24] C. R. Sullivan and S. R. Sanders, "Models for induction machines with magnetic saturation of the main flux path," Conference Record of the 1992 *IEEE Industry Appl. Soc. Ann. Meet.*, pp. 123-131 vol.1, 1992.

[25] Tang Ningping, Wu Hanguang and Qiu Peiji, "A saturation model of induction machine by space vector," ICEMS'2001. *Proceed. Fifth Int. Conf. Elec. Mach. Sys.*, (IEEE Cat. No.01EX501), 2001, pp. 85-88 vol.1, 2001.

[26] M. Bodson and O. Kiselychnyk, "Analysis of Triggered Self-Excitation in Induction Generators and Experimental Validation," in *IEEE Trans. on Energ. Conv.*, vol. 27, no. 2, pp. 238-249, June 2012.

[27] F. Therrien, M. Chapariha and J. Jatskevich, "Constant-Parameter Voltage-Behind-Reactance Induction Machine Model Including Main Flux Saturation," in *IEEE Trans. on Energ. Conv.*, vol. 30, no. 1, pp. 90-102, March 2015.

[28] O. Kiselychnyk, M. Bodson and J. Wang, "Comparison of Two Magnetic Saturation Models of Induction Machines and Experimental Validation," in *IEEE Trans. Ind. Electr.*, vol. 64, no. 1, pp. 81-90, Jan. 2017.

[29] S. Nandi, "A detailed model of induction machines with saturation extendable for fault analysis," in *IEEE Trans. Ind. Appl.*, vol. 40, no. 5, pp. 1302-1309, Sept.-Oct. 2004.

[30] V. Donescu, A. Charette, Z. Yao and V. Rajagopalan, "Modeling and simulation of saturated induction motors in phase quantities," in *IEEE Trans. on Energ. Conv*., vol. 14, no. 3, pp. 386-393, Sept. 1999.

[31] J. O. Ojo, A. Consoli and T. A. Lipo, "An improved model of saturated induction machines," in *IEEE Trans. Ind. Appl.*, vol. 26, no. 2, pp. 212-221, 1990.

[32] J. C. Moreira and T. A. Lipo, "Modeling of saturated AC machines including air gap flux harmonic components," in *IEEE Trans. Ind. Appl.*, vol. 28, no. 2, pp. 343-349, March-April 1992.

[33] B. J. Chalmers and R. Dodgson, "Waveshapes Of Flux Density In Polyphase Induction Motors Under Saturated Conditions," in *IEEE Trans. Pow. Appar. Sys.*, vol. PAS-90, no. 2, pp. 564-569, March 1971.

[34] X. Tu, L. Dessaint, R. Champagne and K. Al-Haddad, "Transient Modeling of Squirrel-Cage Induction Machine Considering Air-Gap Flux Saturation Harmonics," in *IEEE Trans. Ind. Elec.*, vol. 55, no. 7, pp. 2798-2809, July 2008.

[35] S. Moulahoum, O. Touhami, R. Ibtiouen and M. Fadel, "Induction Machine Modeling With Saturation and Series Iron Losses Resistance," 2007 *IEEE Int. Elec. Mach. Driv. Conf.*, Antalya, 2007.

[36] J. M. Aller, D. Delgado, A. Bueno, J. C. Viola and J. A. Restrepo, "Model of the induction machine including saturation," 2013 15th *Eur. Conf. Pow. Electr. Appl.* (EPE), Lille, 2013, pp. 1-8.

[37] M. Carbonieri, N. Bianchi and L. Alberti, "Direct Analysis of Three-Phase Induction Motor Considering Rotor Parameters' Variation and Stator Belt Harmonics Effect," in *IEEE Trans. Ind. Appl*., vol. 56, no. 4, pp. 3559-3570, July-Aug. 2020.

[38] E. Roshandel, A. Mahmoudi, S. Kahourzade and W. Soong, "Analytical Model and Performance Prediction of Induction Motors using Subdomain Technique," 2020 *IEEE Ener. Conv. Cong. Expo.* (ECCE), Detroit, MI, USA, pp. 3815-3822, 2020.

[39] Ansys® Electromagnetics, Release 2020.

[40] T. Yamaguchi, Y. Kawase, M. Shibata, T. Furukawa, & H. Kawano, "3-D Finite Element Analysis of Interbar Current of V-skewed Squirrel-cage Induction Motor Taking into Account of Contact Resistance," *Jour. Japan Soc. Appl. Electromag. And Mech*., vol. 27, no. 1, pp. 146-151, 2019.

[41] Z. Gmyrek, A. Cavagnino and S. Vaschetto, "FEM Analysis of the Inter-Bar Currents in Induction Motors Aimed at Estimating Contact Resistance," 2019 *IEEE Int. Elec. Mach. & Driv. Conf.* (IEMDC), pp. 1532-1538, 2019.